Surface Science 652 (2016) 206–212

Contents lists available at ScienceDirect

Surface Science

journal homepage: www.elsevier.com/locate/susc

Interfacial Cu^+ promoted surface reactivity: Carbon monoxide oxidation reaction over polycrystalline copper–titania catalysts

Sanjaya D. Senanayake [a,*], Naa Adokaley Pappoe [b], Thuy-Duong Nguyen-Phan [a], Si Luo [d], Yuanyuan Li [e], Wenqian Xu [a], Zongyuan Liu [d], Kumudu Mudiyanselage [a], Aaron C. Johnston-Peck [c], Anatoly I. Frenkel [e], Ilana Heckler [d], Dario Stacchiola [a], José A. Rodriguez [a,d]

[a] Chemistry Department, Brookhaven National Laboratory, Upton, NY 11973, United States
[b] The City College of New York, New York, NY 10031, United States
[c] Center for Functional Nanomaterials (CFN), Brookhaven National Laboratory, Upton, NY 11973, United States
[d] Department of Chemistry, Stony Brook University, Stony Brook, NY 11790, United States
[e] Department of Physics, Yeshiva University, New York, NY 10016, United States

ARTICLE INFO

Available online 26 February 2016

Keywords:
Copper
Titania
Interface
Carbon monoxide
Oxidation
Carbon dioxide

ABSTRACT

We have studied the catalytic carbon monoxide (CO) oxidation ($CO + 0.5O_2 \rightarrow CO_2$) reaction using a powder catalyst composed of both copper (5 wt.% loading) and titania (CuO_x–TiO_2). Our study was focused on revealing the role of Cu, and the interaction between Cu and TiO_2, by systematic comparison between two nanocatalysts, CuO_x–TiO_2 and pure CuO_x. We interrogated these catalysts under in situ conditions using X-ray diffraction (XRD), X-ray absorption fine structure (XAFS) and diffuse reflectance infrared Fourier transform spectroscopy (DRIFTS) to probe the structure and electronic properties of the catalyst at all stages of the reaction and simultaneously probe the surface states or intermediates of this reaction. With the aid of several ex situ characterization techniques including transmission electron microscopy (TEM), the local catalyst morphology and structure were also studied. Our results show that a CuO_x–TiO_2 system is more active than bulk CuO_x for the CO oxidation reaction due to its lower onset temperature and better stability at higher temperatures. Our results also suggest that surface Cu^+ species observed in the CuO_x–TiO_2 interface are likely to be a key player in the CO oxidation mechanism, while implicating that the stabilization of this species is probably associated with the oxide–oxide interface. Both in situ DRIFTS and XAFS measurements reveal that there is likely to be a Cu(Ti)–O mixed oxide at this interface. We discuss the nature of this Cu(Ti)–O interface and interpret its role on the CO oxidation reaction.

1. Introduction

Carbon monoxide (CO) is a highly toxic compound that is an essential component in the synthesis gas used in many chemical operations and also a byproduct of numerous industrial and automotive processes which involve the combustion of fuels. Due to ever increasing emission standards, research has focused on limiting or remediating the emissions of this pollutant. CO oxidation has thus become a very important reaction to protect the environment and the health of the general population. The removal of CO can be achieved by the catalytic oxidation process that involves O_2 and also H_2 (CO PROX) conversion into carbon dioxide (CO_2):

$$CO + 0.5O_2 \rightarrow CO_2. \quad (1)$$

This process is commonly used in industry at low temperatures [1] to clean carbon monoxide streams. The CO even at low concentration can affect the use of H_2 as a viable fuel, and CO_2 is a gas that is less toxic to the environment as opposed to carbon monoxide, but is nonetheless a major contributor to greenhouse gases. Typically, the types of catalyst used for this reaction involve expensive precious metals such as Au, Pt, Rh, and Pd and oxide supports such as CeO_x, FeO_x and TiO_x. Studies by Yates and co-workers have shown that the metal-oxide interface plays a determinant role in the low-temperature oxidation of CO on Au–TiO_2 catalysts [2,3]. The key steps in the catalytic CO oxidation process likely involve the following steps:

$$CO\ (g) \rightarrow CO\ (a) \quad (2)$$

$$O_2\ (g) \rightarrow O_2\ (a) \quad (3)$$

$$O_2\ (a) \rightarrow 2O\ (a) \quad (4)$$

$$CO\ (a) + O\ (a) \rightarrow CO_2\ (a) \quad (5)$$

* Corresponding author.
E-mail address: ssenanay@bnl.gov (S.D. Senanayake).

http://dx.doi.org/10.1016/j.susc.2016.02.014
0039-6028/

$$CO\ (a) + 2O\ (a) \rightarrow CO_3\ (a) \quad (6)$$

$$CO\ (g) + O\ (a) \rightarrow CO_2\ (a) \quad (7)$$

$$CO\ (g) + 2O\ (a) \rightarrow CO_3\ (a) \quad (8)$$

$$CO_2\ (a) \rightarrow CO_2\ (g) \quad (9)$$

$$CO_3\ (a) \rightarrow CO_2\ (g) + O(s). \quad (10)$$

Some of these steps involve the Langmuir–Hinshelwood (L–H) mechanism in which both reactants are adsorbed on the catalyst surface in order to form a bimolecular reaction and the Ely–Rideal (E–R) mechanism in which only one reactant is adsorbed firmly on the catalyst while the other strikes the adsorbates from the gas phase in order to form a bond without adsorbing [4]. Between these two mechanisms, the Langmuir–Hinshelwood (L–H) mechanism has been widely proposed yet can be element (catalyst), kinetic (reactant concentration) or thermodynamic (temperature) specific.

Oxide based catalysts have a natural selectivity towards redox processes and their lower costs and high abundance compared to that of pure noble metals such as gold, platinum, silver and palladium make them highly attractive as catalysts [5,6]. In addition, mixed oxides have provided new and unique properties beyond what is obtainable from mono-oxides [7]. These mixed oxides can either be in the form of naturally occurring solid solutions (one oxide inside another) or as one oxide in contact with another at a distinct interfacial boundary [8]. Often this interfacial oxide–oxide synergy can manifest in unique geometrical, chemical or electronic properties and thus influence catalytic selectivity, which can work either cooperatively or passively to enhance catalytic activity and sustain stability [9]. The true nature of this interfacial active sites is highly composition and element specific and also very sensitive to the type of reaction (i.e. oxidizing vs reducing, hydrogenation vs dehydrogenation, dehydration vs dehydrogenation, etc.) where it prevails. Understanding the role of these mixed metal oxide sites and the catalysts that encompass them requires careful and systematic analysis often incorporating in situ methods that are sensitive to the active state under reaction conditions.

The aim of our study is to investigate one such as mixed oxide powder catalyst composed of CuO_x and TiO_2, a cheaper alternative to noble metals, which is highly active for the CO oxidation reaction. In the case of mixtures of CuO_x and TiO_x, there is evidence reported previously of the generation of intermixed materials such as $Cu_xTi_yO_z$ [10–12]. The nature of the stabilization of Cu^+ species in a CuO_x–TiO_x interface and a mixed oxide was investigated systematically over model surfaces using infrared spectroscopy (IR) and proved to be critical for catalyzing the CO oxidation reaction [10] and the epoxidation of propylene [13]. Theoretical models of this system were also studied with careful observations of the nature of the Cu^+ surface species in CuO_x–TiO_x [14]. In this work we explore such an interface in polycrystalline Cu–TiO_2, and also make comparisons with that of a base catalyst, CuO_x, to elucidate the role of Cu^+ and the CuO_x–TiO_2 interface using several in situ characterization techniques. The key questions we hope to answer about the CuO_x–TiO_2 catalyst include: what are the oxidation states of Cu {Cu (0), Cu_2O (1+), CuO (2+)} and Ti species {Ti (0), TiO_2 (4+), Ti_2O_3 (3+)} that prevail during the reaction, which components/sites are the most important/active, and what are their roles in the reaction? As shown by Yates and co-workers for the Au–TiO_2 system [2,3], we also find that an interface provides the best combination of reaction sites for catalyzing CO oxidation.

2. Experimental

2.1. Catalyst preparation

Powders of anatase TiO_2 (Aldrich) were calcined to 500 °C in air flow prior to incorporating a cupric nitrate precursor ($Cu(NO_3)_2$, Aldrich). The 5 wt.% CuO_x–TiO_2 catalyst was prepared by a deposition–precipitation method (DP) using Na_2CO_3 (Alfa Aesar) as the precipitating agent, which was added to the TiO_2 and Cu precursors in order to keep a neutral pH of 7 at 70 °C. In these conditions, the copper precipitated as $Cu(OH)_2$. The Cu/TiO_2 sample was calcined to 500 °C in air flow following the deposition–precipitation process. The reduction experiments of the CuO_x–TiO_2 in CO and the catalytic oxidation of CO were conducted at temperatures lower than 300 °C, much smaller than that of the calcination process at 500 °C. CuO_x samples were calcined in air to 500 °C prior to experiments.

2.2. STEM

The high resolution TEM images of the CuO_x–TiO_2 samples were taken using a high angular annular dark field scanning transmission microscopy (HAADF STEM) instrument. The powder sample was dispersed as a suspension in deionized water, sonicated for 60 s then introduced in drops onto a Holey-C grid and allowed to dry before imaging. Electron energy loss spectroscopy (EELS) and energy disperse X-ray spectroscopy (EDS) chemical maps were acquired on a Hitachi 2700C operated at 200 kV using convergence semi-angles of 23 and 28 mrad, respectively.

2.3. XRD

The phases with long-range order (i.e. crystalline structure) in the catalyst were examined with X-ray Diffraction. The XRD study was carried out on beamline X7B ($\lambda = 0.3196$ Å) of the National Synchrotron Light Source (NSLS) at Brookhaven National Laboratory (BNL). Powder samples of 2–3 mg were loaded into a silica capillary (0.9 mm ID, 1.0 mm OD) mounted in the flow cell system. A Perkin Elmer Amorphous Silicon Detector was used to collect two-dimensional transmission diffraction data, which were subsequently processed with the program Fit2D to obtain XRD profiles. Lattice parameters and phase quantities were analyzed by the Rietveld refinement using the program GSAS.

Temperature-resolved XRD experiments under CO oxidation conditions were also performed at beamline X7B (NSLS). Around 2 mg powder samples were loaded in a 1.0 mm OD amorphous silica capillary installed to a flow reactor. Details of the flow reactor and the experiment setting can be found at Ref. [15]. The sample was pre-oxidized in 5% O_2/He at 300 °C for half an hour and cooled to room temperature. The gas environment was then changed to a mixture of 2.5% CO and 1.25% O_2 balanced in He. A stepwise heating program was used: the sample was heated to 100, 150, 200, and 250 °C consecutively and held at each temperature step for 30 min. Between two steps, the heating rate was 10 °C/min. XRD data were continuously collected throughout the experiment.

2.4. XANES/XAFS

XANES and EXAFS were used to detect the possible existence of amorphous or non-crystalline phases in the catalyst. Cu K-edge XANES data were collected in transmission mode at the beamline X19A (NSLS) using ionization chamber detectors for measuring incident and transmitted beam intensities. In addition, a third ionization chamber was used to detect the beam through a reference Cu foil, for energy calibration and alignment purposes. The flow micro-reactor and the sample were the same ones used in the XRD experiment. The fresh catalyst powder samples from the same batch were initially treated with helium at a flow rate of 10 ml/min at room temperature. Then 5% O_2/He mixture was introduced and the EXAFS data were collected.

Afterwards, the CO oxidation reaction studies were performed under a 0.5% CO/0.25% O_2/He mixture and at the same temperatures as in XRD experiment described above, while collecting EXAFS data. Details of the flow micro-reactor, the experimental setup that combined XAFS and Raman spectroscopy capability, and the description of the results of such combination can be found in Ref. [16]. In this work we focus on the structure of the pre-reaction state that was described previously as "unique" and not understood [16,17].

2.5. DRIFTS

DRIFTS data were collected on CuO_x–TiO_x and pure CuO_x under CO oxidation conditions using a Bruker Equinox 55 FTIR spectrometer equipped with a modified Harrick Praying Mantis DRIFTS cell that was connected to a gas flow system and a mass spectrometer. Carbon monoxide and oxygen with concentrations of 5% and 20%, in helium respectively, were allowed to flow through the sample. The gas flow rate used in this study was 10 cm^3/min. Stepwise heating and cooling with an increment of 50 °C, starting from room temperature up to 250 °C were applied. The temperature was held for 20–30 min at each step where the temperature reading is stabilized. The composition of the outflow gas was analyzed with a mass spectrometer.

3. Results

3.1. Local morphology

The STEM images shown in Fig. 1 show the local morphology of an as prepared CuO_x–TiO_2 catalyst that is composed of small copper oxide nanoparticles (~2–6 nm) located on TiO_2 (~10–50 nm). The CuO_x appears highly dispersed on the TiO_2 particles and the Z-contrast between the Cu vs Ti allows us to distinguish the two oxides from each other. The STEM image on the right shows a representative spherical CuO_x nanoparticle (~2 nm) that wets TiO_2.

The interface between the Cu and Ti oxides appears relatively abrupt and there is no indication of the formation of a third phase, however, this does not necessarily preclude chemical intermixing.

3.2. Bulk structure

The ex situ powder diffraction pattern of the CuO_x–TiO_2 system shown in Fig. 2 indicates the presence of three crystalline structures associated with CuO_x and the anatase and rutile phases of TiO_2. The peak intensity variations indicate that the catalyst is composed predominantly of anatase rather than rutile TiO_2. The calculated compositions of the crystalline structures of anatase, rutile and CuO are 85%, 13% and 2%, respectively. The nominal loading of CuO_x is 5% thus there is likely to be either 3% non-crystalline or very finely dispersed CuO_x species present on this catalyst.

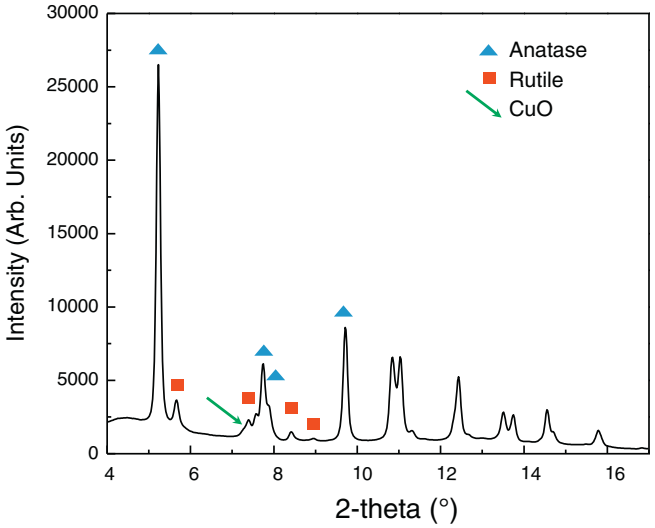

Fig. 2. X-ray Diffraction (XRD) of as prepared CuO_x–TiO_x catalyst.

3.3. CO oxidation reactivity

A comparison of the reactivity of CuO_x and CuO_x–TiO_2 is presented in Fig. 3. The left panel shows the mass spectroscopic profile of CO (black), O_2 (green), and CO_2 (red) gases during CO oxidation in a micro-reactor at incremental heating to temperatures of 100–250 °C followed by cooling. The data shows the production of CO_2 (red) at temperatures that coincide with the consumption of CO and O_2, identifying catalytic activity of both catalysts. The comparative rate of CO_2 production for CuO_x is small at 100 °C, with an earlier onset of reaction for CuO_x–TiO_2. This trend is prevalent with increasing temperatures with a better performance of the CuO_x–TiO_2 catalyst. At 150 °C almost near identical deactivation of both catalysts is observed with a slow decrease in CO_2 production as a function of time. Notably, at 200 °C the CuO_x–TiO_x catalyst shows good stability against a gradually deactivating CuO_x. At 250 °C both catalysts are comparable in rate of conversion and also stability. The right panel exhibits the relative yields of CO_2 product over

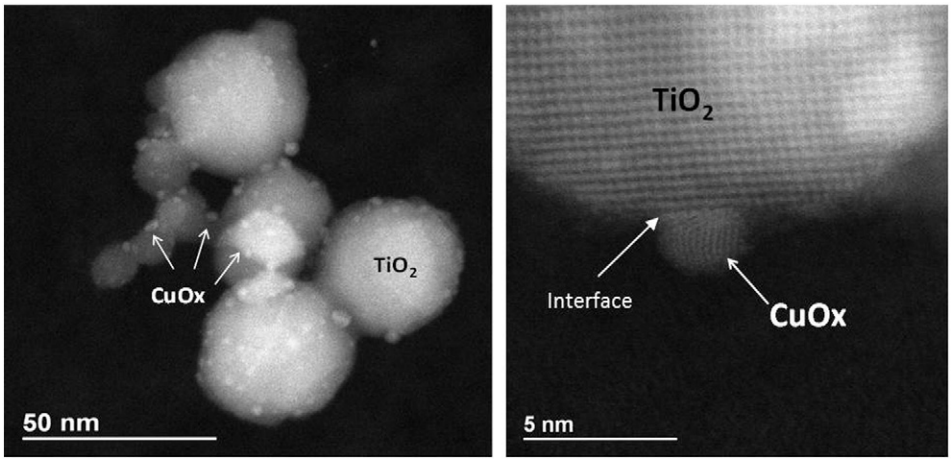

Fig. 1. Scanning transmission electron micrographs (HAADF–STEM) of as prepared CuO_x–TiO_x catalyst.

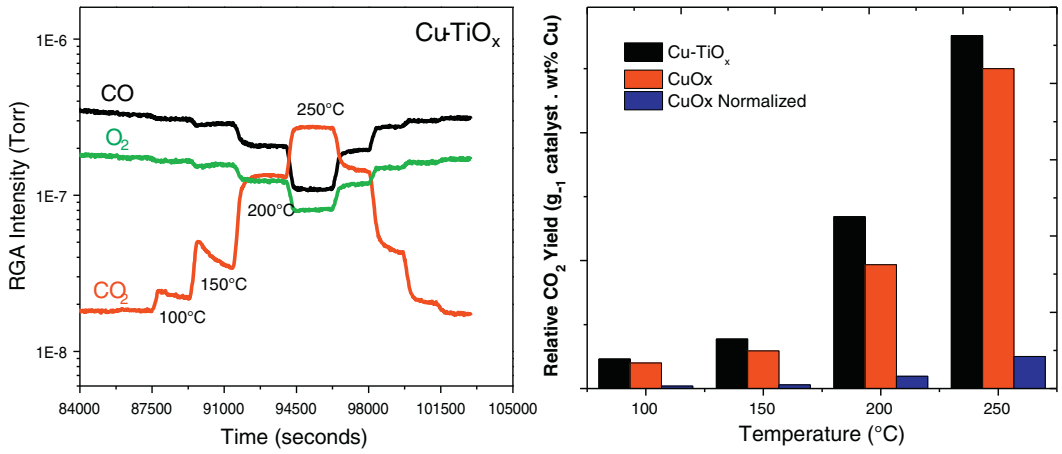

Fig. 3. CO oxidation activity of CuO_x and CuO_x–TiO_x catalysts at 100 °C, 150 °C, 200 °C and 250 °C: (left) mass spectroscopic profile of residual gases during CO oxidation over CuO_x–TiO_x; (right) relative CO_2 yield over CuO_x and CuO_x–TiO_x catalysts, with comparison to a CuO_x that is normalized with respect to Cu loading for comparison.

CuO_x reference and CuO_x–TiO_2 catalyst. A comparison is also made with the CuO_x sample normalized per unit loading (CuO_x normalized) with respect to the 5 wt.% CuO_x–TiO_2. It is clear that mixed oxide catalyst shows higher activity than that of the reference regardless of reaction temperature.

3.4. In situ XRD

We studied the changes to the crystalline bulk structure of CuO_x–TiO_x during this reaction using in situ XRD (Fig. 4) and monitored simultaneously the reactant to product conversion. A stack plot of five XRD profiles at each temperature step is shown in Fig. 4 from 25 °C, 100 °C, 150 °C, 200 °C and 250 °C. No change occurred to the structures of the TiO_2 phases (anatase and rutile). In contrast, the CuO phase, represented by its (002) peak at 7.3° of 2–θ, which is seen as a shoulder to the rutile (101) peak at 7.4°, decreased in intensity from 200 to 250 °C (inset, Fig. 4). The weight fraction of the CuO_x phase as a function of time and temperature is plotted in the inset of Fig. 4. As the amount of CuO_x dropped, no other Cu-related phases like Cu_2O and Cu metal could be positively identified by XRD. Several possibilities may be considered for this newly formed Cu-phase including that they have (i) adopted very small particle sizes, (ii) are transformed to amorphous or poorly crystalline structure in nature, or (iii) intermixing (CuO_x and TiO_2) into the formation of a $Cu_xTi_yO_z$ structure that is not visible to the detection by XRD. It is interesting to note that massive reduction of CuO occurred at 200 °C (Fig. 4), when the production of CO_2 dramatically increased. Clearly, the conversion of CuO to CuO_{1-x} led to the formation of an active phase responsible for the CO oxidation activity. From previous experiments with Cu–CeO_x for CO oxidation under nominally similar conditions we identified Cu(I) as the active component for this reaction [18].

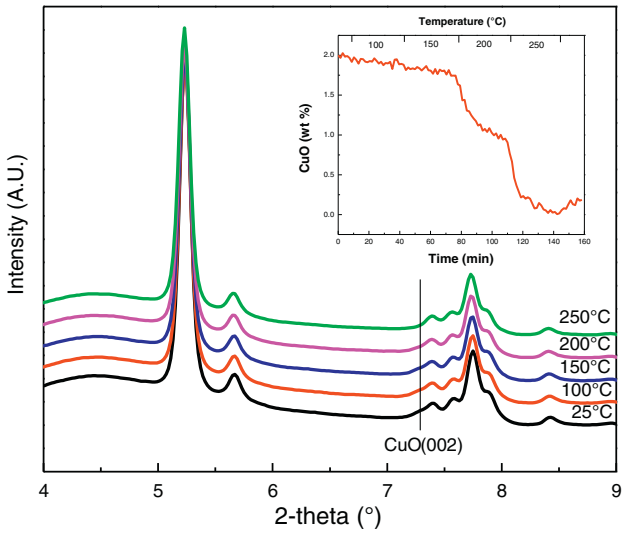

Fig. 4. In situ XRD of CuO_x–TiO_x catalysts at 100 °C, 150 °C, 200 °C and 250 °C, inset of CuO_x fraction as a function of temperature. Experimental conditions: powder sample loaded in an amorphous silica capillary installed to a gas flow reactor. XRD patterns were collected continuously during *Operando* CO oxidation that was described in detail above.

3.5. In situ DRIFTS

To understand the surface chemistry occurring on this CuO_x–TiO_2 catalyst we performed in situ DRIFTS under CO oxidation conditions similar to measurements described earlier. Fig. 5 shows the infrared spectra recorded while CuO_x (left-side panel) and CuO_x–TiO_2 (right-side panel) are heated to elevated temperatures incrementally (25, 50, 100, 150, 200 and 250 °C) under CO oxidation conditions.

In the panel for CuO_x–TiO_2 in Fig. 5 (right-side), an intense peak appears at 2100–2120 cm^{-1} for the CO adsorbed on Cu^+ sites. This peak overlaps with one of the gas phase CO bands (the CO gas phase feature is centered at 2143 cm^{-1}). It is notably absent on the CuO_x catalyst (left-side panel). For CuO_x–TiO_2, the CO adsorbed on Cu^+ peak gradually decreases as the temperature increases and is small at 250 °C. The decrease of the Cu^+–CO peak with temperature is probably a consequence of a reduction in the number of adsorbed CO molecules. In fact, the concentration of Cu^+ in the system is probably increasing as a consequence of intermixing in the oxide–oxide interface (see inset in Fig. 4). It has been reported that Cu^+–carbonyls have higher frequency than 2120 cm^{-1}, ranging from 2164 to 2230 cm^{-1} [19]. The adsorbed CO on Cu^+ observed in our study is different from organometallic carbonyl compounds and hence frequencies are different. It is well known that adsorption of CO on metallic Cu is weak and not observed under the condition used in our study on powder catalysts but CO adsorbed on Cu^+ is stable and gives a peak around 2120 cm^{-1} [20,21]. Herein, no evidence showing the presence of two different types of adsorbed CO has been observed. Moreover, at 50 °C a new peak appears at 2349 cm^{-1} in Fig. 5 corresponding to the gas phase CO_2 indicative of the start of the CO oxidation reaction.

The left-side panel in Fig. 5 shows the infrared spectra recorded with CuO_x as it is heated to different temperatures under identical CO oxidation conditions. At 25 °C, only gas phase CO bands centered at

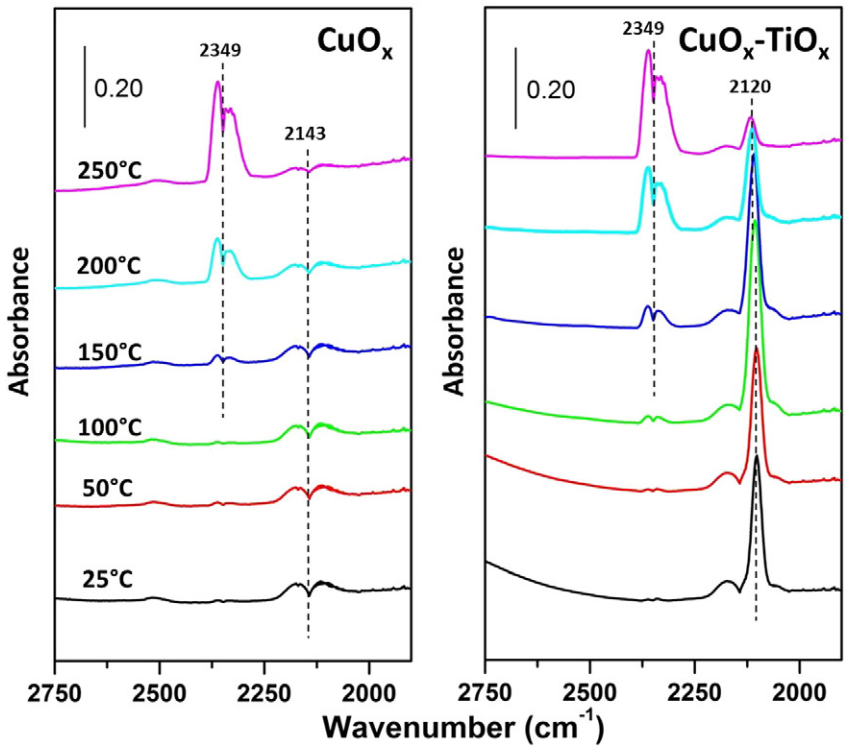

Fig. 5. DRIFTS data from CuO_x (left) and CuO_x–TiO_x (right) catalysts at 25 °C, 50 °C, 100 °C, 150 °C, 200 °C and 250 °C under CO oxidation reaction conditions. Experimental conditions: DRIFTS cell was connected to a gas flow system and a mass spectrometer. The reactant composition was 5% CO and 20% O_2 balanced in He with 10 cm^3/min.

2143 $cm^{-1}$are seen. At 150 °C, a peak appears at 2349 cm^{-1} for the gas phase CO_2 indicating the beginning of the CO oxidation reaction. The intensity of the peak for gas phase CO_2 at 2349 cm^{-1} increased as the temperature is raised. A similar trend is observed in the panel for CuO_x–TiO_2 but, at any given temperature, the intensity for the features for CO_2 formation is always larger on the mixed-oxide system.

These DRIFTS data agree well with the in situ XRD and reactivity data presented earlier and show that there is a strong correlation between the activity of both CuO_x and CuO_x–TiO_2 to the consumption of CO + O_2 and the production of CO_2. We can confirm that the process involves a transformation of CuO to CuO_{1-x} based on the XRD and XAFS data and the likely presence of CO–Cu^+. The nature of the Cu^+ species can be further correlated to studies we have performed previously on CuO_x–TiO_2 model surfaces where an intermixed $Cu_xTi_yO_z$ bound CO was identified and may prevail on this surface as an active ingredient for this reaction [10,12].

3.6. Local structure and electronic properties of Cu in CuO_x–TiO_2

Fig. 6 shows the normalized Cu K-edge XANES (left) and Fourier transformed $k^2\chi(k)$ (right) data of 5 wt.% CuO_x/TiO_2 collected before the CO oxidation reaction (under O_2 at 25 °C), and the reference bulk oxides: CuO and Cu_2O. Both XANES and EXAFS spectra of CuO_x–TiO_2 are distinctly different from those of standard copper oxides, which indicate that the local environment of Cu in the CuO_x–TiO_2 sample is different from that in the oxides. This species is suggested to be in +2 valence state based on the existence of a weak pre-edge peak at about 8979 eV in XANES spectrum (Fig. 6 (left)). This pre-edge peak appears in most Cu(II) compounds and could be regarded as a signature for a divalent copper. It represents the quadrupole-allowed 1s → 3d transition, suggesting the presence of a hole in the copper 3d orbitals in CuO_x–TiO_2 sample. For Cu(0) and Cu(I) compounds with $3d^{10}$ configuration, such pre-edge peak should not be expected. Other than the pre-edge region,

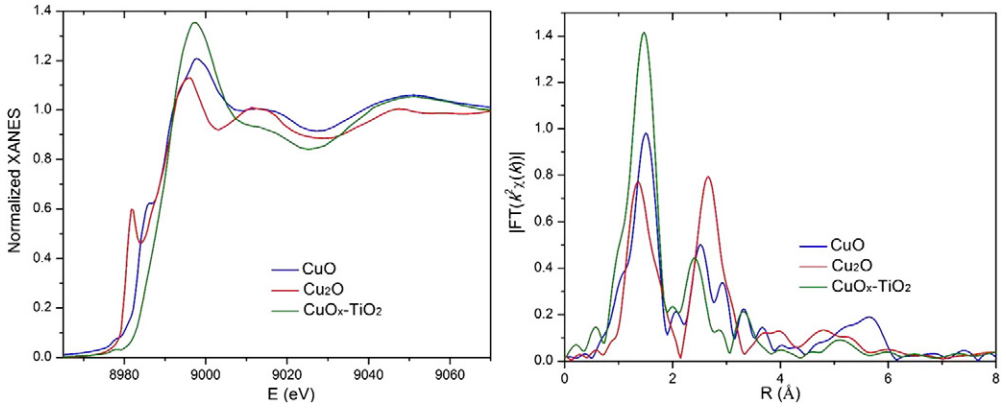

Fig. 6. XANES (left) and EXAFS (right) data of the 5 wt.% CuO_x–TiO_2 sample before the CO oxidation reaction, at 25 °C, under O_2 flow. XAFS spectra of copper oxides were reproduced from previous work [16] and shown here for comparison.

spectral differences can also be observed in rising edge and maximum in XANES spectrum between CuO_x–TiO_2 and copper oxides. Compared to XANES spectra of copper oxides, the shoulder at the rising edge is absent and the intensity of the maximum is higher in XANES spectrum of CuO_x–TiO_2. The shoulder at the rising edge and the maximum are usually assigned to the dipole allowed 1s → 4p transition, and their intensities and positions/energies associate with neighboring atomic geometry [22,23]. In Cu_2O, each copper atom forms two collinear bonds with oxygen atoms which results in the split of 4p orbitals into $4p_{xy}$ and $4p_z$. The shoulder at the rising edge is assigned to Cu 1s → $4p_{xy}$ transition while the maximum represents Cu 1s → $4p_z$ transition. In CuO, each copper atom is surrounded by four nearest oxygen atoms and forms a nearly planar structure, which also causes the split of 4p orbitals to $4p_{xy}$ and $4p_z$. Due to the $3d^9$ configuration, the shoulder at the rising edge is assigned to Cu 1s → $4p_{xy}$ + shakedown transition and the maximum is ascribed to 1s → $4p_z$ transition [24,25]. For CuO_x–TiO_2, one likely reason for the absence of the shoulder peak and the presence of intense white line in XANES spectrum is the modification of local geometry around Cu, which in turn changes the 4p configuration. The unique local atomic structure around Cu in CuO_x–TiO_2 can also be observed in EXAFS spectra (Fig. 6 (right)). For all three spectra, there are two distinct peaks. One locates at about 1.5 Å and another at about 2.5 Å. The former is ascribed to Cu–O contribution and the latter to Cu–M (metal) contribution. It can be clearly seen that the Cu–O peak in the spectrum of CuO_x–TiO_2 is quite intense and the position of Cu–M peak shifts to lower distance compared with those of Cu_2O and CuO. To understand the structural nature of such new copper species in CuO_x–TiO_2 sample, EXAFS data for CuO_x–TiO_2 were analyzed and quantitative results for coordination numbers (N) and bond distances (R) for Cu–O and Cu–M bonds were obtained by fitting theoretical EXAFS signals to experimental data. Four different models of local environment of Cu were used for data analysis: (i) Cu–O and Cu–Cu (the latter contribution was extracted from the CuO structure), (ii) Cu–O and Cu–Cu (the latter contribution was extracted from Cu metal), (iii) Cu–O and Cu–Ti (Cu–Ti path was created by substituting Ti by Cu in anatase TiO_2 lattice), and (iv) Cu–O, Cu–Ti and Cu–Cu. Among these four models, only the third model gave a good fit (Fig. 7). This model describes the substitutional mechanism of incorporation of Cu into TiO_2 support. To this copper species, the coordination number of Cu–O pair is 4.1 ± 0.5 and Cu–Ti pair: 1.4 ± 0.8. The distances of Cu–O and Cu–Ti bonds are 1.942 ± 0.009 Å and 2.94 ± 0.02 Å, respectively.

In this third model all Cu–O pairs were assumed to have identical bond length and disorder. That assumption is needed, in order to lower the number of variables in the fit and satisfy Nyquist criterion [26]. From the analysis of a standard CuO system we know that such approximation causes an unphysical reduction of the coordination number indicating that different Cu–O bonds do, in fact, have different disorder factors. If approximated by a constant disorder an apparent reduction of coordination number follows [27]. Therefore, the coordination number of ca. 4 obtained for the Cu(Ti)–O sample can be also underestimated. Our XANES analysis (vide infra) shows that, indeed, an octahedral (N = 6) environment of Cu is more consistent with experimental data.

As mentioned above, spectral features along the rising edge in XANES reflect local geometry around Cu atoms. Such geometrical characteristics can be obtained by first principle modeling of Cu K-edge XANES signals and are expected to be in good agreement with those derived from EXAFS analysis, for both XANES and EXAFS modeling to be valid. The XANES spectra were calculated using FEFF 9 code [28]. Simulations were first performed on cooper oxides (CuO and Cu_2O) for finding optimized conditions for FEFF calculations. For all calculations, identical parameters were used to account for experimental broadening in all spectra that were all measured using the same experimental setups. In calculating the XANES spectrum of the CuO_x–TiO_2 sample, the same model was used as in EXAFS analysis. In this model, Cu substitutes Ti atom and thus bonds with six oxygen atoms in octahedral symmetry (two of them are along the axial direction). The calculated XANES spectra are shown in Fig. 8. The lack of the shoulder at the rising edge, the right shift of the rising edge and the higher intensity of the maximum, all these features shown in the experimental data of CuO_x–TiO_2 compared to copper oxides (Fig. 6 (left)) are also exhibited in the calculated spectrum for Cu(Ti)–O models designed with symmetric octahedral geometry. On the basis of the EXAFS and XANES results, it can thus be concluded that for the CuO_x–TiO_2 sample, Cu substitutes Ti atom and adopts the same geometry as Ti in the anatase lattice. Additionally, the fact that the shoulder peak shows up for Cu_2O and CuO, systems that possess linear and square planar geometries, respectively, while disappears for Cu(Ti)–O with octahedral geometry, suggests that additional neighboring oxygen atoms along axial direction in the local structure of Cu in the catalyst sample are responsible for the absence of the shoulder peak caused by the splitting of the 4p orbitals.

4. Discussion

Both CuO_x–TiO_2 and CuO_x showed activity for the CO oxidation reaction, but CuO_x–TiO_2 has improved CO_2 production even at lower temperature, extended stability and better performance per Cu loading. Our results identify that the likely source of this chemistry may be attributed to several possibilities, including better dispersion of small Cu nanoparticles, the interaction between Cu and Ti either at the interface or as a mixed oxide, and the prevalence of Cu^+ on the catalyst surface.

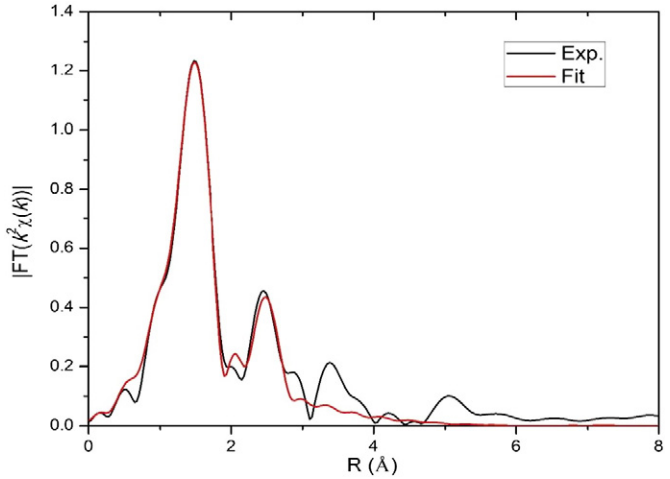

Fig. 7. EXAFS data and fit. The fitting k range is 3–11 $Å^{-1}$ and R range is 1.0–2.8 Å.

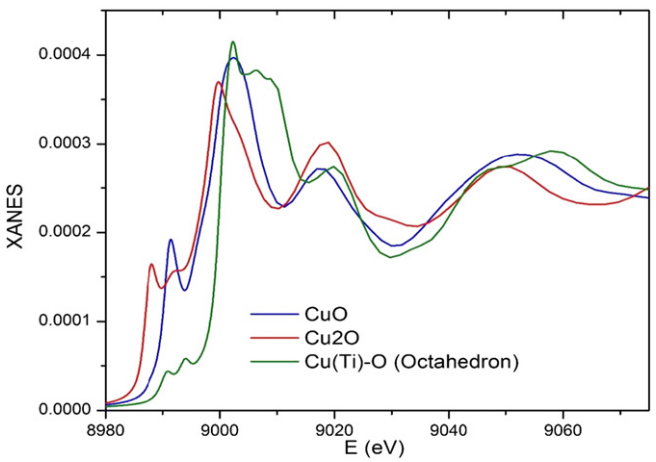

Fig. 8. Simulated XANES spectra for CuO, Cu_2O and Cu(Ti)–O with octahedral geometry.

The surface chemistry and likely mechanism observed on both surface appear to be strikingly different. We demonstrate that the active catalyst surface structure can be used to tailor reaction pathways. This Cu^+ species is not observed on CuO_x despite some CO oxidation activity. The location of the Cu^+ species may likely be at the interface between Cu and Ti oxides where a mixed oxide of $Cu_xTi_yO_z$ forms and we propose is an active agent in CO oxidation. The evidence for this species forming at reaction conditions is clear from the assignment of the CO–Cu^+ species (2100–2120 cm^{-1}) from in situ DRIFTS experiments, which was also implicated in studies over well-defined surface models [10] and DFT [14] for CO oxidation. However, it is important to note that in our polycrystalline CuO_x–TiO_2 catalyst, this Cu^+ rich interface is not optimized, despite high dispersion of Cu, and the likely active sites are limited to the contact points or perimeters around the Cu nanoparticles on TiO_2. We propose that a strategy to further improve CO oxidation activity would be to atomically disperse Cu, and extend the CuO_x–TiO_2 interaction further through stabilization of smaller nanostructured units rich in Cu^+. This may be an important insight for even other heterogeneous oxidation reactions, implicating that the presence of the Cu^+ sites facilitates an improved pathway for catalytic activity.

Previous studies by Yates and co-workers showed the importance of the metal–oxide interface for the low temperature oxidation of CO on Au/TiO_2 [2,3]. An oxide–oxide interface is probably responsible for the high CO oxidation activity of CuO_x–TiO_2. At an interface the formation of chemical bonds can modify the electronic and chemical properties of a material enhancing its catalytic activity. Furthermore, at an interface one can combine elements that have different chemical behaviors which can work in a cooperative way in different steps of a catalytic process [2,3]. The results in our present study exhibit the higher activity of Cu–TiO_x for the CO oxidation and the stability of Cu^+ under the reaction conditions as similar to the previous studies on model systems [10,12]. The stability of Cu^+ in model systems is due to the formation of $CuTiO_x$ mixed oxide. Therefore, the comparison of results on powder and model systems suggests that the formation of mixed oxide on powder system leads to the stabilization of Cu^+ which enhances the activity for CO oxidation.

5. Conclusions

We have studied the catalytic CO oxidation to CO_2 using a novel mixed–oxide catalyst composed of CuO_x and TiO_2 and compared it to unsupported CuO_x. This mixed-oxide catalyst is more active for this reaction than either CuO_x or TiO_2 on its own. With the use of XRD, TEM and DRIFTS we were able to identify the local morphology, bulk structure and surface states that prevailed when the CO and O_2 reacted to produce CO_2. We discovered that the CuO_x–TiO_2 has a unique structure that helped to improve the CO oxidation reaction, and that the interface between the CuO_x–TiO_2 as an intermixed oxide ($Cu_xTi_yO_z$) provides for the stabilization of CO–Cu^+ that is likely to be an important part of this reaction.

Notes

The authors declare no competing financial interest.

Acknowledgments

The research carried out in this manuscript was performed at Brookhaven National Laboratory, supported by the U.S. Department of Energy, Office of Science, Office of Basic Energy Sciences, and Catalysis Science Program under contract no. DE-SC0012704. This work used resources of the National Synchrotron Light Source (NSLS) and the Center for Functional Nanomaterials (CFN), that are DOE Office of Science User Facilities. AIF and YL gratefully acknowledge funding of their work by the U.S. DOE grant no. DE-FG02-03ER15476. The authors acknowledge the support the facilities provided at the Synchrotron Catalysis Consortium (U.S. DOE grant no. DE-SC0012335).

References

[1] J.S. Spendelow, J.D. Goodpaster, P.J.A. Kenis, A. Wieckowski, J. Phys. Chem. B 110 (2006) 9545.
[2] I.X. Green, W. Tang, M. Neurock, J.T. Yates Jr., Science 333 (2011) 736.
[3] I.X. Green, W. Tang, M. Neurock, J.T. Yates Jr., Angew. Chem. Int. Ed. 50 (2011) 10186.
[4] R.S. Johnson, A. DeLaRiva, V. Ashbacher, B. Halevi, C.J. Villanueva, G.K. Smith, S. Lin, A.K. Datye, H. Guo, Phys. Chem. Chem. Phys. 15 (2013) 7768.
[5] N.O. Savage, S.A. Akbar, P.K. Dutta, Sensors Actuators B Chem. 72 (2001) 239.
[6] G. Xanthopoulou, G. Vekinis, Appl. Catal., B 19 (1998) 37.
[7] D.J. Stacchiola, S.D. Senanayake, P. Liu, J.A. Rodriguez, Chem. Rev. 113 (2013) 4373.
[8] A.C. Johnston-Peck, S.D. Senanayake, J.J. Plata, S. Kundu, W. Xu, L. Barrio, J. Graciani, J.F. Sanz, R.M. Navarro, J.L.G. Fierro, E.A. Stach, J.A. Rodriguez, J. Phys. Chem. C 117 (2013) 14463.
[9] S. Luo, T.-D. Nguyen-Phan, A.C. Johnston-Peck, L. Barrio, S. Sallis, D.A. Arena, S. Kundu, W. Xu, L.F.J. Piper, E.A. Stach, D.E. Polyansky, E. Fujita, J.A. Rodriguez, S.D. Senanayake, J. Phys. Chem. C 119 (2015) 2669.
[10] A.E. Baber, X. Yang, H.Y. Kim, K. Mudiyanselage, M. Soldemo, J. Weissenrieder, S. Senanayake, A. Al-Mahboob, J.T. Sadowski, J. Evans, J.A. Rodriguez, P. Liu, F.M. Hoffmann, J.G. Chen, D.J. Stacchiola, Angew. Chem. Int. Ed. 53 (2014) 5336.
[11] D.J. Stacchiola, Acc. Chem. Res. 48 (2015) 2151.
[12] K. Mudiyanselage, S. Luo, H.Y. Kim, X. Yang, A.E. Baber, F.M. Hoffmann, S. Senanayake, J.A. Rodriguez, J.G. Chen, P. Liu, D.J. Stacchiola, Catal. Today 263 (2016) 4.
[13] X. Yang, S. Kattel, K. Xiong, K. Mudiyanselage, S. Rykov, S.D. Senanayake, J.A. Rodriguez, P. Liu, D.J. Stacchiola, J.G. Chen, Angew. Chem. Int. Ed. 54 (2015) 11946.
[14] H.Y. Kim, P. Liu, J. Phys. Chem. C 119 (2015) 22985.
[15] J.A. Rodriguez, R. Si, J. Evans, W. Xu, J.C. Hanson, J. Tao, Y. Zhu, Catal. Today 240 (2015) 229.
[16] A. Patlolla, P. Baumann, W. Xu, S.D. Senanayake, J.A. Rodriguez, A.I. Frenkel, Top. Catal. 56 (2013) 896.
[17] A.I. Frenkel, Q. Wang, N. Marinkovic, J.G. Chen, L. Barrio, R. Si, A.L. Camara, A.M. Estrella, J.A. Rodriguez, J.C. Hanson, J. Phys. Chem. C 115 (2011) 17884.
[18] S.Y. Yao, W.Q. Xu, A.C. Johnston-Peck, F.Z. Zhao, Z.Y. Liu, S. Luo, S.D. Senanayake, A. Martínez-Arias, W.J. Liu, J.A. Rodriguez, Phys. Chem. Chem. Phys. 16 (2014) 17183.
[19] S.H. Strauss, J. Chem. Soc., Dalton Trans (2000) 1.
[20] J.C. Hanson, R. Si, W. Xu, S.D. Senanayake, K. Mudiyanselage, D. Stacchiola, J.A. Rodriguez, H. Zhao, K.A. Beyer, G. Jennings, K.W. Chapman, P.J. Chupas, A. Martínez-Arias, Catal. Today 229 (2014) 64.
[21] S. Yao, K. Mudiyanselage, W. Xu, A.C. Johnston-Peck, J.C. Hanson, T. Wu, D. Stacchiola, J.A. Rodriguez, H. Zhao, K.A. Beyer, K.W. Chapman, P.J. Chupas, A. Martínez-Arias, R. Si, T.B. Bolin, W. Liu, S.D. Senanayake, ACS Catal. 4 (2014) 1650.
[22] L.S. Kau, D.J. Spira-Solomon, J.E. Penner-Hahn, K.O. Hodgson, E.I. Solomon, J. Am. Chem. Soc. 109 (1987) 6433.
[23] S.E. Shadle, J.E. Penner-Hahn, H.J. Schugar, B. Hedman, K.O. Hodgson, E.I. Solomon, J. Am. Chem. Soc. 115 (1993) 767.
[24] C.H. Chou, W.F. Pong, I.N. Lin, S.F. Tsai, Chin. J. Phys. 29 (1991) 263.
[25] N. Kosugi, H. Kondoh, H. Tajima, H. Kuroda, Chem. Phys. 135 (1989) 149.
[26] E.A. Stern, Phys. Rev. B Condens. Matter 48 (1993) 9825.
[27] A. Yevick, A.I. Frenkel, Phys. Rev. B 81 (2010) 115451.
[28] J.J. Rehr, J.J. Kas, F.D. Vila, M.P. Prange, K. Jorissen, Phys. Chem. Chem. Phys. 12 (2010) 5503.